HHS Public Access

Author manuscript

ACS Chem Biol. Author manuscript; available in PMC 2019 April 20.

Published in final edited form as:

ACS Chem Biol. 2018 April 20; 13(4): 1013–1020. doi:10.1021/acschembio.8b00199.

Determination of the subcellular localization and mechanism of action of ferrostatins in suppressing ferroptosis

Michael M. Gaschler[a], **Fanghao Hu**[a], **Huizhong Feng**[b], **Andreas Linkermann**[c], **Wei Min**[a,§], and **Brent R. Stockwell**[a,b,§]

[a]Department of Chemistry, Columbia University, New York, NY 10027

[b]Department of Biological Sciences, Columbia University, New York, NY 10027

[c]Medical Clinic III, Division of Nephrology, Carl Gustav Carus University Hospital at the Technical University Dresden, Dresden 01309, Germany

Abstract

Ferroptosis is a form of non-apoptotic cell death characterized by the unchecked accumulation of lipid peroxides. Ferrostatin-1 and its analogs (ferrostatins) specifically prevent ferroptosis in multiple contexts, but many aspects of their molecular mechanism of action remain poorly described. Here, we employed stimulated Raman scattering (SRS) microscopy coupled with small vibrational tags to image the distribution of ferrostatins in cells, and found that they accumulate in lysosomes, mitochondria, and endoplasmic reticulum. We then evaluated the functional relevance of lysosomes and mitochondria to ferroptosis suppression by ferrostatins, and found that neither is required for effective ferroptosis suppression.

Introduction

Preventing cell death may be an effective strategy for treating degenerative diseases and injury. Although cell death can occur in an unregulated manner during classic necrosis, or accidental cell death, such death is often carried out by one of several molecular programs, which are collectively referred to as regulated cell death, in that they can be modulated by pharmacological or genetic manipulation. Compounds that prevent regulated cell death can be useful in multiple contexts, making them valuable tools to treat disease and injury.

Ferrostatin-1 is a potent and selective small-molecule inhibitor of ferroptosis, a form of non-apoptotic, iron-dependent, regulated cell death involving lipid peroxidation.[1, 2] Ferrostatin-1 and its analogs (ferrostatins) prevent ferroptosis in various models of neurodegeneration,[1–3] acute kidney injury,[4, 5] intracerebral hemorrhage,[6] and other degenerative conditions,[2]

[§]Co-corresponding authors: wm2256@columbia.edu, bstockwell@columbia.edu.

Author Contributions

M.M.G., F.H, W.M., B.R.S., contributed to the writing of the manuscript; all authors have given their approval of the final version of the manuscript. M.M.G., F.H., A.L., B.R.S., and W.M. designed research. M.M.G., F.H., H.F., performed research.

Supporting Information

Supporting information, consisting of additional methods and four figures, is available free of charge via the internet at http://pubs.acs.org.

suggesting the potential of ferrostatins as therapeutic agents. Significant exploration of the structure-activity relationship (SAR) of ferrostatins has led to analogs with increased potency and metabolic stability;[2, 4, 7] even so, many aspects of the mechanism of ferroptosis itself, and its suppression by ferrostatins remain to be elucidated.

The correlation between increased lipophilicity and increased potency was one of the first trends discovered in exploring the SAR of ferrostatins. Increasing the lipophilicity of the hydrocarbon moiety on either one of the arylamines led to ferrostatins with greater potency.[1] Additionally, it is worth noting that all active ferrostatin analogs are reducing agents that are able to reduce the stable radical DPPH.[1, 2] Structural modifications that lack such reducing behavior prevent compounds from suppressing ferroptosis. Together, these observations led to the hypothesis that ferrostatins function as lipophilic antioxidants that use their large lipophilic group to anchor into cellular membranes, where they reduce lipid hydroperoxides, or act as radical trapping antioxidants.[8]

We sought to gain deeper insight into the mechanism of ferrostatins to better understand ferroptosis and to aid in the development of new ferrostatins with improved properties. To do so, we harnessed an emerging bio-orthogonal imaging technique known as stimulated Raman scattering (SRS) microscopy coupled with small vibrational tags to visualize ferrostatins in live cells. We used an integrated strategy of exploring the structure-*distribution*-activity relationship, by iteratively varying the structures of ferrostatin analogs and examining the corresponding intracellular distribution and drug potency. We found that ferrostatins accumulate in specific sub-cellular regions, including lysosomes, mitochondria, and endoplasmic reticulum, but not the plasma membrane or nucleus. Accumulation of ferrostatins in mitochondria and lysosomes, however, did not contribute to ferroptosis suppression.

Results

Ferrostatins accumulate in lysosomes, mitochondria, and endoplasmic reticulum

The potency of ferrostatins has been suggested to derive from their ability to anchor in lipid membranes, thereby allowing them to reduce lipid hydroperoxides, or trap radical intermediates in lipid peroxidation.[2] Supporting this, the rate of radical trapping by ferrostatin-1 was enhanced 7.6-fold in liposomes relative to a nonpolar solvent.[8] We sought to image the distribution of ferrostatins in live cells in order to determine whether they preferentially localize to subcellular locations, such as specific membrane environments.

Conventional approaches to imaging the cellular distribution of small molecules involve covalent attachment of a fluorescent dye. For a compound as small as ferrostatin-1, we were concerned that covalent attachment of a bulky fluorescent dye would significantly alter its native activity and localization due to the large size of fluorescent tags. To circumvent this, we employed the emerging stimulated Raman scattering (SRS) microscopy to visualize ferrostatin distribution in living cells. By attaching small vibrational tags only a few atoms in size with characteristic vibrational frequencies in the silent region of a typical cellular Raman spectrum, bio-orthogonal chemical imaging by SRS microscopy achieves live-cell imaging of bioactive molecules with high sensitivity and specificity in a quantitative manner.

[9] Alkynes are promising SRS vibrational tags due to their strong Raman signal, lack of chemical reactivity in cells, small size, and have been successfully used for drug imaging.[10] Compared to single alkynes, conjugated alkynes (*e.g.,* a diyne) further enhance the SRS signal, allowing higher detection sensitivity and lower concentrations of the probe compound.[11, 12]

Given these considerations, we designed and synthesized diyne ferrostatin analog **2** (Figure 1A). Because of the functional tolerance of ferrostatins to extensive substitution at the 4 position,[2] we hypothesized that incorporation of a diyne moiety at this position would not significantly alter the potency of compound **2** relative to the parent ferrostatin-1. To maintain the lipophilicity required for anti-ferroptotic activity, the diyne moiety of **2** was capped with a highly lipophilic n-butyl group. The calculated octanol/water partition coefficient (cLogP) of compound **2** was 3.78, making it slightly more lipophilic than ferrostatin-1 (cLogP 3.2).[2] To validate the potency and activity of compound **2,** we treated ferroptosis-sensitive HT-1080 fibrosarcoma cells with a lethal dose of the ferroptosis inducer erastin, and a serial dilution of ferrostatin-1 or compound **2** (Figure 1B). We found that compound **2** suppressed ferroptosis with a potency similar to ferrostatin-1, confirming that the diyne tag did not significantly affect the anti-ferroptotic activity of the original compound.

Having verified the anti-ferroptotic activity of probe **2,** we aimed to image its distribution in living cells. First, we confirmed that the diyne tag of probe **2** shows a distinct peak at 2262 cm^{-1} within the cell Raman-silent window (Supplemental figure 1). Next, HT-1080 cells were treated with **2** and erastin simultaneously, and imaged by SRS microscopy after 6 h of incubation (Figure 1C). Most strikingly, **2** accumulated in large puncta throughout the cytoplasm, with lesser accumulation through the remainder of the cytoplasm. Notably, no significant amount of **2** was detected in the nucleus or in the plasma membrane, within the limits of SRS sensitivity. To test if this pattern of accumulation was specific to cells undergoing ferroptosis, we incubated HT-1080 cells with probe **2** in the absence of erastin (Figure 1D). We did not observe a significant change in its distribution, indicating that the pattern of ferrostatin localization does not depend on whether or not ferroptosis has been initiated, as might be expected. To ensure this pattern of localization was not specific to HT-1080 cells, we tested diyne **2** in the immortalized pancreatic cancer line Panc-1. Similar to HT-1080 cells, Panc-1 cells treated with diyne ferrostatin analog **2** also showed strong accumulation in puncta throughout the cytosol and little accumulation within the nucleus both in the presence and absence of erastin (Supplemental figure 2).

We sought to determine if this observed distribution was due to accumulation of probe **2** at specific organelles. We hypothesized that the large puncta might correspond to accumulation within lysosomes. HT-1080 cells were treated with probe **2** for 6 h, followed by 30 min with the lysosome-targeted fluorescent dye LysoTracker, and both compounds were imaged within the same cells by correlative SRS and fluorescence microscopy (Figure 1E). The LysoTracker signal showed partial overlap with the large puncta from probe **2**, suggesting that these sites of ferrostatin accumulation were indeed lysosomes.

In addition to lysosomes, the mitochondria and endoplasmic reticulum (ER) have also been hypothesized to play roles in ferroptosis,[1, 13] and were additional sites of localization of

probe **2**. We therefore sought to examine whether probe **2** accumulated at either of these organelles. HT-1080 cells were treated with **2** and both a mitochondria-specific and ER-specific fluorescent dye (Figure 1F). Though the lower signal intensity of **2** at these sites indicated that **2** was present at lower concentrations in both of these locations than in lysosomes, **2** showed a clear pattern of overlap with the mitochondria-specific fluorescent dye Mito Tracker Deep Red. Due to the diffuse nature of ER network, it was unclear if the widespread distribution of **2** was due to specific accumulation within ER, but the image we observed was nonetheless consistent with ER accumulation of ferrostatins, given that it was not as diffuse at the extent of cytosol. Thus, based on the linear concentration dependence of SRS signal, we concluded that **2** accumulates primarily in lysosomes, with additional localization in mitochondria and ER, but did not show detectable concentrations in the plasma membrane or the nucleus.

Accumulation at Lysosomes Reduces the Potency of Ferrostatins

The role of lysosomes in ferroptosis is unclear. Earlier studies reported a burst of reactive oxygen species (ROS) in lysosomes of cells undergoing ferroptosis,[14] but lysosomal membrane permeabilization, a feature of other forms of oxidative cell damage, was not observed in cells treated with erastin.[2] Additionally, lysosomes store iron imported by endocytosis of transferrin, a process critical for ferroptosis.[15] Correspondingly, the membrane-impermeable iron chelator DFO likely protects against ferroptosis by chelating iron accumulated in lysosomes *via* endocytosis.[16]

We hypothesized that ferrostatins accumulate in lysosomes because of the lysosomotropic effect.[17] In their neutral form, small molecules with weakly basic sites (generally aromatic or aliphatic amines) can freely diffuse through lipid membranes and between cellular compartments. In acidic lysosomes (pH 4.5–5.0), basic groups are protonated and unable to diffuse out because of the resulting positive charge. In this way, molecules can be trapped in lysosomes, even if their biological target is elsewhere in a cell.[18] In support of our hypothesis, we calculated the acidity of the conjugate acids of each amine on ferrostatin-1 in an aqueous environment. We found that the conjugate acid of the unsubstituted arylamine has a pK_a of 4.6, suggesting it can be protonated in the lysosome. Given the basic aromatic amines in ferrostatins and the observed high levels of accumulation of probe **2** within lysosomes, we examined whether lysosomal accumulation of ferrostatins was critical to their mechanism of ferroptosis rescue or if lysosomotropism prevents ferrostatins from reaching their necessary targets.

We first incubated HT-1080 cells with a lethal dose of erastin and a serial dilution of ferrostatin-1, as well as 0 (vehicle only), 5, or 10 μM chloroquine (Figure 2A). Chloroquine is a classic lysosomotropic agent, and is protonated in lysosomes, thus raising lysosomal pH, reducing the extent of molecular trapping by the lysosomotropic effect for other compounds. We found that co-treatment of cells with ferrostatin-1 and chloroquine caused an increase in the potency (lower EC_{50}) of ferrostatin-1 in a chloroquine dose-dependent manner (Figure 2A).

Since preventing ferrostatin accumulation in lysosomes increased ferrostatin potency (Figure 2A), we hypothesized that promoting ferrostatin accumulation in lysosomes would

correspondingly decrease their potency (*i.e.,* require a higher concentration of ferrostatin to suppress ferroptosis). We designed and synthesized ferrostatins **3** and **4**, which each contain a basic morpholine group, a moiety commonly used to target molecules to lysosomes (Figure 2B)[19]. Ferrostatin **4** has a cLogP of 1.94, slightly less lipophilic than ferrostatin-1 and ferrostatin **2,** while ferrostatin **3** was more lipophilic with a cLogP value of 2.07. Though such physiochemical changes might change many properties of a compound (e.g. increased non-specific protein binding), we hypothesized that changes in the potency of compounds **3** and 4 would mainly arise from the protonation of the morpholine nitrogen in the lysosome, thereby increasing the amount of ferrostatin sequestration in this organelle. Indeed, both ferrostatins **3** and **4** showed an eight-fold loss in potency in their ability to rescue cells from erastin-induced ferroptosis (Figure 2C), relative to ferrostatin-1. In addition, co-treatment of cells with LysoTracker dye and either **2** or **4** revealed that, as designed, ferrostatin **4** accumulates strongly in lysosomal compartments (Figure 2D), confirming that the decrease in potency is correlated with increased sequestration in lysosomes. Cumulatively, these data suggest that reducing the basicity of the ferrostatin amines could improve potency by reducing lysosomal sequestration, although a careful balance between basicity and reduction potential of amines needs to be considered for developing more effective ferroptosis inhibitors. With the ability to perform direct SRS imaging of drug distribution inside cells, this methodology is an example of exploring the structure-*distribution*-activity relationship, and correlating this with the structure-activity relationship.

Mitochondria are not required for ferroptosis or ferroptosis rescue by ferrostatin-1

Since ferrostatin analog **2** showed accumulation in mitochondria, we sought to determine whether mitochondria are necessary for ferroptosis, as well as for ferroptosis rescue by ferrostatins. ROS generated by the mitochondrial electron transport chain do not contribute to ferroptosis, as cells lacking mitochondrial DNA are still sensitive to ferroptosis.[1] Still, ACSL4-dependent alterations in mitochondrial morphology are observed in cells undergoing ferroptosis,[1, 20, 21] and the nitroxide antioxidant XJB-5-131, which is targeted to mitochondria, is a more potent inhibitor of ferroptosis than untargeted analogs.[22]

To examine the necessity of mitochondria for ferroptosis, we generated mitochondria-deficient cells, using a previously reported mitophagy protocol.[23] The E3 ligase parkin causes the elimination of mitochondria lacking a membrane potential *via* mitophagy, a macroautophagic process specific to mitochondria.[23, 24] We generated stably transfected HT-1080 cells expressing YFP-parkin or mCherry-parkin (Figure 3A). Loss of membrane potential was induced by treatment with the uncoupling agent carbonyl cyanide *m*-chlorophenyl hydrazine (CCCP). Following treatment of YFP-parkin-expressing cells or mCherry-parkin-expressing cells with CCCP for 48 h, we examined the levels of the mitochondria specific proteins tom20 and cytochrome C (Figure 3B). Parkin-expressing cells had highly diminished levels of both proteins after 48 hours of CCCP treatment, confirming the elimination of most mitochondria. Extensive mitochondrial depletion within 48 h has been observed in other cell types using this approach.[23, 24] We also observed near-complete absence of the complex 1 genes Mt-Nd1 and Mt-Nd2 following CCCP treatment (Figure 3C and 3D). YFP-parkin CCCP-treated cells also showed a decrease in

immunofluorescence signal when imaged for mitochondria-specific proteins COX IV and HSP60, while wild-type cells showed no significant change (supplemental figure 3A). Electron microscopy imaging of YFP-parkin-expressing cells treated with CCCP confirmed a significant decrease in the number of observable mitochondria by TEM (Figure 3E and supplemental figure 3B). YPF-parkin cells depleted of mitochondria also showed a large increase in the abundance of endoplasmic reticulum and/or Golgi bodies (supplemental figure 3B). Cells depleted of mitochondria showed a greatly decreased growth rate, but were nonetheless persistent in cell culture over multiple days.

To examine the necessity of mitochondria for ferroptosis, we treated YFP-Parkin-expressing HT-1080 cells with a panel of ferroptosis-inducing compounds. All ferroptosis inducers tested effectively killed cells depleted of mitochondria in a similar oxidative, dose-dependent manner to cells harboring mitochondria (Figure 3F, Supplemental figure 3C, and Supplemental figure 4), indicating that the presence of mitochondria is not necessary for ferroptosis. Staurosporine, an inducer of mitochondria-dependent apoptosis, caused no loss in viability over all concentrations tested, confirming that mitochondria had been effectively and functionally removed, and that staurosporine-induced apoptosis requires mitochondria, as expected. Notably, inhibitors of system x_c^- (erastin and IKE) both became somewhat less potent following CCCP treatment (i.e. after mitophagy), while RSL3 and FIN56, which target GPX4, both became somewhat more potent after mitophagy. When CCCP was withdrawn at the time of ferroptosis induction, these potency shifts for FIN56 and RSL3 did not change significantly, confirming that these changes in potency were the direct result of mitophagy and not an off-target effect of the presence of CCCP (supplemental figure 3C). The level of GPX4 protein, a master regulator of ferroptosis, did not decrease in mitochondria-depleted HT-1080 cells relative to wildtype HT-1080 cells treated with CCCP (supplemental figure 3D). Additionally, wild-type HT-1080 cells treated with CCCP were still sensitive to staurosporine and showed no change in sensitivity to ferroptosis inducers, other than the modest resistance to system x_c^- inhibitors noted above (supplemental figure 3E).

We then evaluated the ability of ferroptosis-suppressing compounds to prevent ferroptosis in cells depleted of mitochondria. Both ferrostatin-1 and iron chelators (deferoxamine and ciclopirox olamine) were able to prevent erastin-induced ferroptosis in a dose-dependent manner (supplemental figure 3F and 3G), confirming that the mechanism of erastin lethality was consistent with ferroptosis in CCCP-treated YFP-parkin cells. We evaluated the potency of ferrostatin-1 in YFP-parkin-transfected HT-1080 cells following mitophagy (Figure 3G). Cells were treated with a lethal concentration of either the class 1 ferroptosis inducer erastin or the class 2 ferroptosis inducer RSL3,[16] and a serial dilution of ferrostatin-1. In both cases, ferrostatin-1 became moderately more potent following mitophagy, indicating that mitochondria are not required for ferroptosis suppression by ferrostatins.

The data above suggest that mitochondria are not necessary for ferroptosis induction and neither mitochondria nor lysosomes are necessary for ferroptosis induction or ferrostatin action, despite the prominent accumulation of ferrostatin-1 in these organelles. Together with the overall distribution of diyne ferrostatin **2** observed by SRS (Figure 1C), this suggests that the location in which ferrostatin exerts its anti-ferroptotic action is likely the

ER, unless there is another relevant location with very low levels of ferrostatin present, below the detection limit of SRS. The hypothesis that ER is the site of ferrostatin action is supported by the increased potency of ferrostatin-1 in post-mitophagy cells, which showed greater ER abundance (supplemental figure 3B).

Discussion

In this study, we sought to gain insight into the mechanism of ferroptosis suppression by ferrostatin-1. The ability of ferrostatin-1 to act as a reducing agent was one of the earliest observed properties of the compound,[1] and served as the basis for initial hypotheses about its mechanism of action.[2]

We sought to understand where ferrostatin-1 accumulates inside cells, as enrichment within a ferroptosis-relevant organelle could explain the high potency of Fer-1. By employing SRS microscopy coupled with small vibrational tags, we observed significant localization of ferrostatins within lysosomes, mitochondria, and the endoplasmic reticulum, and minimal accumulation within the nucleus and plasma membrane. We hypothesized that, as the nexus of iron import and trafficking, lysosomes might play a critical role in ferroptosis. Instead we found that accumulation within lysosomes actually decreased the overall potency of ferrostatins, while preventing ferrostatin accumulation in lysosomes by chloroquine treatment increased ferrostatin-1 potency.

To examine the role of ferrostatin localization at mitochondria, we generated a stably transfected cell line that was depleted of mitochondria. We found that mitochondria-deficient cells were still sensitive to ferroptosis, and could still be rescued by ferrostatins and iron chelators. It should be noted that a very small number of mitochondria may still remain in these cells, and we cannot yet rule out a role for such a residual population of mitochondria in initiating a chain reaction of lipid peroxidation; nonetheless, we can state that mitochondria are not the primary site of lipid peroxidation during ferroptosis. By varying the structures of ferrostatin analogues, examining the corresponding intracellular distribution and drug potency, and using this information to guide iterative rounds of structure design, we are adopting a strategy of integrating the structure-distribution-activity relationship. Such a methodology can be applied to study the mechanism of other drugs.

Together, these data suggest that ferrostatin accumulation within the endoplasmic reticulum could be critical to ferroptosis suppression, and that the ER may also be critical to ferroptosis initiation. The ER lumen is an oxidative environment and might initiate ferroptosis as a consequence of ER-related oxidative stress. Alternately, the ER is the source of lipids for most membranes in other organelles and contains more than half of all lipid bilayers in any given cell.[25] Therefore, it is possible that ferrostatin accumulation within the ER is the most efficient strategy to maintain overall peroxide tone within cellular membranes; ER localization would allow ferrostatins to prevent oxidation of the majority of cellular lipids, thereby decreasing lipid peroxide abundance.

Methods

Cell lines and media

HT-1080 cells were obtained from ATCC and grown in DMEM with glutamine and sodium pyruvate (Corning 10-013) supplemented with 10% Heat-Inactivated FBS, 1% non-essential amino acids (Invitrogen), and 1% penicillin-streptomycin mix (Invitrogen). Panc-1 cells were obtained from ATCC and grown in DMEM with glutamine and sodium pyruvate (Corning 10-013) supplemented with 10% Heat-Inactivated FBS, and 1% penicillin-streptomycin mix (Invitrogen). Phoenix-AMPHO (ATCC: CRL-3213) were grown in DMEM supplemented with 10% heat-inactivated FBS, 1% penicillin-streptomycin mix (Invitrogen), and 2 mM L-glutamine. All cells were maintained in a humidified environment at 37 ºC and 5% CO_2 in a tissue incubator.

Ferroptosis rescue assay

3,000 cells were seeded per well in black, clear bottom 384-well plates (Corning) and allowed to adhere overnight. The next day, the medium was replaced with 50 μL of growth medium and 5 μL medium containing erastin (10 μM) or (1*S*, 3*R*)-RSL3 (2 μM) and a dilution series of the ferroptosis-suppressing compound. 24 h later, 6.1 μL of Presto Blue (Thermo-Fisher) was added. Cells were incubated for an additional 5 h, and the Presto Blue fluorescence intensity was measured using a Victor X5 plate reader (PerkinElmer)(ex/em 530/590). Background (no cells) fluorescence was subtracted and the resulting fluorescence intensities were averaged between biological replicates. From these data, dose-response curves and EC_{50} values were computed using Prism 7.0 (GraphPad). For mitophagy experiments, YFP-Parkin transfected HT-1080 cells were cultured in medium containing 12.5 μM CCCP for 24 h. Cells were then trypsinized, suspended and seeded into white, opaque-bottom 384-well plates (corning) at a density of 3,000 cells per well in 50 μL medium containing 12.5 μM CCCP and allowed to adhere for 24 additional hours (48 h CCCP treatment in total). The medium was either kept or replaced with CCCP-free medium (herein designated “+CCCP” or “+Mitophagy −CCCP”, respectively), and treated with 5 μL medium containing molecules as described above. Viability was assayed using CellTiter-Glo® (Promega) according to the manufacturer’s protocol. Luminesence was read on a Victor X5 plate reader and data were analyzed as described above.

Computational methods

Computational determination of octanol/water partition coefficient (ClogP) was performed in MOE 2016.0802 using the Slog P function (Chemical Computing Group). Compound pKa was calculated using Jaguar pKa (Schrödinger Inc.)

SRS microscopy

An integrated laser source (picoEMERALD, Applied Physics & Electronics, Inc.), is used to produce both a Stokes beam (1064 nm, 6 ps, intensity modulated at 8 MHz) and a tunable pump beam (720 to 990 nm, 5–6 ps) at 80 MHz repetition rate. Two spatially and temporally overlapped beams are coupled into an inverted multiphoton laser-scanning microscope (FV1200MPE, Olympus) with optimized near-IR throughput. Both beams are focused on the

cell samples through either a 25× water objective (XLPlan N, 1.05 N.A. MP, Olympus) or a 60× water objective (UPlanAPO/IR, 1.2 N.A., Olympus), and collected with an high N.A. oil condenser lens (1.4 N.A., Olympus) after the sample. By blocking the Stokes beam with a high O.D. bandpass filter (890/220 CARS, Chroma Technology), only the pump beam is collected with a large area Si photodiode (FDS1010, Thorlabs) reverse-biased by 64 DC voltage. The output current of photodiode is filtered electronically (KR 2724, KR electronics), terminated with 50 Ω, and demodulated with a RF lock-in amplifier (SR844, Stanford Research Systems) with near shot-noise-limited sensitivity. The stimulated Raman loss signal at each pixel is sent to the analog interface box (FV10-ANALOG, Olympus) of the microscope to generate the image. All images (512 × 512 pixels) are acquired with 30 μs time constant at the lock-in amplifier and 100 μs pixel dwell time (~27 s per frame). Measured after the objectives, 12 mW pump power and 40 mW Stokes power are used to image the 2940 cm^{-1} channel. 48 or 88 mW pump beam and 120 mW Stokes beam are used to image the 2262 cm^{-1} and 2000 cm^{-1} channels.

Spontaneous Raman spectroscopy

Raman spectra are collected on a confocal Raman microscope (Xplora, Horiba Jobin Yvon with LabSpec 6 software) at room temperature. The sample is excited through a 50 × air objective (MPlan N, 0.75 N.A., Olympus) with a 532-nm diode laser (27 mW after the objective). The acquisition time for ferrostatin 2 in DMSO solution was 20 s.

Sample preparation for SRS and fluorescence imaging of live cells

HT-1080 and Panc-1 cells are seeded on glass coverslips in 4-well plates with ~1 mL of culture media one day before experiment. After the treatment, cells are washed with phosphate buffered saline (PBS, Sigma) for 3 times and the coverslip with cells is assembled into a chamber filled with PBS solution for imaging. Fluorescence imaging is performed using the Olympus FV1200 confocal microscope with standard laser excitation and bandpass filter set for each dye. All images are assigned color and analyzed by ImageJ.

Cell Transfection

Phoenix-AMPHO (ATCC: CRL-3213) cells were seeded in a 6-well plate at 800,000 cells/well. After 20 h, the medium was changed to 800 uL Opti-mem in each well. A solution of Lipofectamine 2000 (6 uL) in 100 uL Opti-mem media (reduced serum media) and YFP-Parkin-IRES-zeocin (Addgene, #61728) plasmid (2.5 ug) or mCherry-Parkin-IRES-zeocin (Addgene, #61727) plasmid (2.5 ug) each in 100 uL Opti-mem media were combined and incubated 20 min at room temperature, then added to each well. After 4 h, 1 mL Opti-mem with 20% FBS was added to each well. 24 h later, the medium was replaced with 10% FBS, 1% penicillin-streptomycin mix (Invitrogen), 2 mM L-glutamine in DMEM. The next day the supernatant was collected three times spaced 4 h apart and polybrene was added (1:1000 dilution). The supernatant was filtered (0.45 μm filters) and added to HT1080 cells seeded at 160,000 cells per well (6-well dish) in 2 mL portions spaced 4 h apart. After 48 h, the cells were trypsinized and re-seeded in medium containing zeocin (400 μg/mL). After 2 weeks of selection with zeocin, the HT1080 cells were then used in subsequent assays, and cultured in standard HT-1080 medium.

Western blotting

Cells were seeded in growth medium and left untreated or treated with 12.5 μM CCCP, after 24 h the medium was washed out and replaced with fresh medium containing 12.5 μM CCCP and incubated 24 h more (48 h total). Medium was then aspirated from each dish and cells washed twice with cold PBS. Cells were lysed in 60 μL RIPA buffer with protease inhibitors. Unlysed cells and debris were pelleted for 15 min at 16,000 xg at 4˚C. Samples were separated using SDS-PAGE and transferred to nitrocellulose membranes. Transfer was performed using the iBlot system (Invitrogen). Membranes were treated with Li-COR Odyssey blocking buffer for 1 h at room temperature, then incubated with primary antibody in a 1:1 solution of PBS-T and Li-COR odyssey blocking buffer overnight at 4˚C. Following three 5 min washes in PBS-T, the membrane was incubated with secondary antibodies (1:3000) in a 1:1 solution of PBS-T and Li-COR Odyssey blocking buffer for 1 h at room temperature. Following three 5 min washes in PBS-T, membranes were scanned using the Li-COR Odyssey Imaging System. Antibodies for cytochrome c (BD Biosciences), tom20 (Santa Cruz) and parkin (Sigma-Aldrich) were detected using a goat anti-rabbit or goat anti-mouse IgG antibody conjugated to an IRdye at 800CW and 680CW conjugated, respectively (Li-COR Biosciences).

Quantitative PCR (qPCR)

Cells with and without CCCP treatment were detached from 100 mm culture dishes, and 3 million cells were collected as a pellet by centrifuging 1,000 rpm for 5 min. Total cellular DNA sample was prepared using DNeasy Blood & Tissue Kit (QIAGEN) according to manufacturer’s instruction. Primers for qPCR were designed with NCBI Primer-BLAST. qPCR was performed using Power SYBR Green Master Mix (Applied Biosystems) in a 96-well format, in triplicate, using viiA7 Real-Time PCR system (Life Technologies). Comparative analysis (ΔΔCt analysis) was performed with Pecam and 18s as internal reference genes.

Immunofluorescence

Cells with and without CCCP treatment were fixed with 4% formaldehyde for 20 minutes at room temperature. Following fixation, cells were permeabilized in PBS-T buffer (0.1% Triton in PBS) for 10 min and blocked in blocking buffer (5% normal goat serum in PBT) for 1 hour at room temperature. Cells were incubated overnight at 4˚C with anti-COX IV antibody (Abcam) and anti-HSP60 antibody (Abcam) 1/1000 diluted in blocking buffer. Cells were washed three 5 min in PBS-T (0.05% Tween20 in PBS) then incubated with goat anti-mouse IgG antibody conjugated to an IRdye at 680CW (Li-COR Biosciences) for 1 h at room temperature. Cells were washed three 5 min in PBS-T and mounted on slides with ProLong™ Diamond Antifade Mountant with DAPI (Thermo Fisher). Slides were analyzed using Zeiss LSM 700 confocal microscope. Fluorescence intensities were quantified with Image J software.

Electron microscopy

Fixed cells were incubated with 2.5% glutaraldehyde and 2% paraformaldehyde in 100 mM cacodylate buffer (pH 7.4) overnight. Samples were then treated with 1% osmium tetroxide

in 100 mM cacodylate buffer for 1 h, washed in distilled water four times (10 min/wash), and then treated with 1–2% aqueous uranyl acetate overnight at 4°C in the dark. Samples were then washed and sequentially dehydrated with increasing concentrations of acetone (20, 30, 50, 70, 90, and 100%) for 30 min each, followed by three additional treatments with 100% acetone for 20 min each. Samples were then infiltrated with increasing concentrations of Spurr's resin (25% for 1 h, 50% for 1 h, 75% for 1 h, 100% for 1 h, 100% overnight at room temperature), and then incubated overnight at 70°C in a resin mold. Sections of 50–90 nm were cut on a Leica ultramicrotome with a diamond knife. Imaging then took place using an FEI Talos F200X operating at 200kV.

Supplementary Material

Refer to Web version on PubMed Central for supplementary material.

Acknowledgments

M. Gaschler was supported by the NIH Training Program in Molecular Biophysics Grant T32GM008281. B. Stockwell was supported by NIH/NCI (R35CA209896 and P01CA087497). W. Min acknowledges support from the NIH Director's New Innovator Award, NIH R01 (Grant EB020892), the Alfred P. Sloan Foundation and the Camille and Henry Dreyfus Foundation. Electron microscopy studies were performed by C. Goulbourne. We would like to acknowledge Columbia University's Nanoscience Initiative for the use of its shared facilities, and the Fu Foundation School of Engineering and Applied Science and the Faculty of Arts & Sciences for their support of the CNI Facilities.

References

1. Dixon SJ, Lemberg KM, Lamprecht MR, Skouta R, Zaitsev EM, Gleason CE, Patel DN, Bauer AJ, Cantley AM, Yang WS, Morrison B 3rd, Stockwell BR. Ferroptosis: an iron-dependent form of nonapoptotic cell death. Cell. 2012; 149:1060–1072. [PubMed: 22632970]
2. Skouta R, Dixon SJ, Wang J, Dunn DE, Orman M, Shimada K, Rosenberg PA, Lo DC, Weinberg JM, Linkermann A, Stockwell BR. Ferrostatins inhibit oxidative lipid damage and cell death in diverse disease models. J Am Chem Soc. 2014; 136:4551–4556. [PubMed: 24592866]
3. Kabiraj P, Valenzuela CA, Marin JE, Ramirez DA, Mendez L, Hwang MS, Varela-Ramirez A, Fenelon K, Narayan M, Skouta R. The neuroprotective role of ferrostatin-1 under rotenone-induced oxidative stress in dopaminergic neuroblastoma cells. Protein J. 2015; 34:349–358. [PubMed: 26385697]
4. Linkermann A, Skouta R, Himmerkus N, Mulay SR, Dewitz C, De Zen F, Prokai A, Zuchtriegel G, Krombach F, Welz PS, Weinlich R, Vanden Berghe T, Vandenabeele P, Pasparakis M, Bleich M, Weinberg JM, Reichel CA, Brasen JH, Kunzendorf U, Anders HJ, Stockwell BR, Green DR, Krautwald S. Synchronized renal tubular cell death involves ferroptosis. Proc Natl Acad Sci U S A. 2014; 111:16836–16841. [PubMed: 25385600]
5. Martin-Sanchez D, Ruiz-Andres O, Poveda J, Carrasco S, Cannata-Ortiz P, Sanchez-Nino MD, Ruiz Ortega M, Egido J, Linkermann A, Ortiz A, Sanz AB. Ferroptosis, but Not Necroptosis, Is Important in Nephrotoxic Folic Acid-Induced AKI. J Am Soc Nephrol. 2017; 28:218–229. [PubMed: 27352622]
6. Li Q, Han X, Lan X, Gao Y, Wan J, Durham F, Cheng T, Yang J, Wang Z, Jiang C, Ying M, Koehler RC, Stockwell BR, Wang J. Inhibition of neuronal ferroptosis protects hemorrhagic brain. JCI Insight. 2017; 2:e90777. [PubMed: 28405617]
7. Hofmans S, Vanden Berghe T, Devisscher L, Hassannia B, Lyssens S, Joossens J, Van Der Veken P, Vandenabeele P, Augustyns K. Novel Ferroptosis Inhibitors with Improved Potency and ADME Properties. J Med Chem. 2016; 59:2041–2053. [PubMed: 26696014]

8. Zilka O, Shah R, Li B, Friedmann Angeli JP, Griesser M, Conrad M, Pratt DA. On the Mechanism of Cytoprotection by Ferrostatin-1 and Liproxstatin-1 and the Role of Lipid Peroxidation in Ferroptotic Cell Death. ACS Cent Sci. 2017; 3:232–243. [PubMed: 28386601]
9. Wei L, Hu F, Chen Z, Shen Y, Zhang L, Min W. Live-Cell Bioorthogonal Chemical Imaging: Stimulated Raman Scattering Microscopy of Vibrational Probes. Acc Chem Res. 2016; 49:1494–1502. [PubMed: 27486796]
10. Wei L, Hu F, Shen Y, Chen Z, Yu Y, Lin CC, Wang MC, Min W. Live-cell imaging of alkyne-tagged small biomolecules by stimulated Raman scattering. Nat Methods. 2014; 11:410–412. [PubMed: 24584195]
11. Yamakoshi H, Dodo K, Palonpon A, Ando J, Fujita K, Kawata S, Sodeoka M. Alkyne-tag Raman imaging for visualization of mobile small molecules in live cells. J Am Chem Soc. 2012; 134:20681–20689. [PubMed: 23198907]
12. Lee HJ, Zhang W, Zhang D, Yang Y, Liu B, Barker EL, Buhman KK, Slipchenko LV, Dai M, Cheng JX. Assessing cholesterol storage in live cells and C. elegans by stimulated Raman scattering imaging of phenyl-Diyne cholesterol. Sci Rep. 2015; 5:7930. [PubMed: 25608867]
13. Dixon SJ, Patel DN, Welsch M, Skouta R, Lee ED, Hayano M, Thomas AG, Gleason CE, Tatonetti NP, Slusher BS, Stockwell BR. Pharmacological inhibition of cystine-glutamate exchange induces endoplasmic reticulum stress and ferroptosis. Elife. 2014; 3:e02523. [PubMed: 24844246]
14. Torii S, Shintoku R, Kubota C, Yaegashi M, Torii R, Sasaki M, Suzuki T, Mori M, Yoshimoto Y, Takeuchi T, Yamada K. An essential role for functional lysosomes in ferroptosis of cancer cells. Biochem J. 2016; 473:769–777. [PubMed: 26759376]
15. Gao M, Monian P, Quadri N, Ramasamy R, Jiang X. Glutaminolysis and Transferrin Regulate Ferroptosis. Mol Cell. 2015; 59:298–308. [PubMed: 26166707]
16. Cao JY, Dixon SJ. Mechanisms of ferroptosis. Cell Mol Life Sci. 2016; 73:2195–2209. [PubMed: 27048822]
17. Deduve C, Debarsy T, Poole B, Trouet A, Tulkens P, Vanhoof F. Lysosomotropic Agents. Biochem Pharmacol. 1974; 23:2495. [PubMed: 4606365]
18. Fu D, Zhou J, Zhu WS, Manley PW, Wang YK, Hood T, Wylie A, Xie XS. Imaging the intracellular distribution of tyrosine kinase inhibitors in living cells with quantitative hyperspectral stimulated Raman scattering. Nat Chem. 2014; 6:614–622. [PubMed: 24950332]
19. Dong B, Song X, Wang C, Kong X, Tang Y, Lin W. Dual Site-Controlled and Lysosome-Targeted Intramolecular Charge Transfer-Photoinduced Electron Transfer-Fluorescence Resonance Energy Transfer Fluorescent Probe for Monitoring pH Changes in Living Cells. Anal Chem. 2016; 88:4085–4091. [PubMed: 26987045]
20. Friedmann Angeli JP, Schneider M, Proneth B, Tyurina YY, Tyurin VA, Hammond VJ, Herbach N, Aichler M, Walch A, Eggenhofer E, Basavarajappa D, Radmark O, Kobayashi S, Seibt T, Beck H, Neff F, Esposito I, Wanke R, Forster H, Yefremova O, Heinrichmeyer M, Bornkamm GW, Geissler EK, Thomas SB, Stockwell BR, O'Donnell VB, Kagan VE, Schick JA, Conrad M. Inactivation of the ferroptosis regulator Gpx4 triggers acute renal failure in mice. Nat Cell Biol. 2014; 16:1180–1191. [PubMed: 25402683]
21. Doll S, Proneth B, Tyurina YY, Panzilius E, Kobayashi S, Ingold I, Irmler M, Beckers J, Aichler M, Walch A, Prokisch H, Trumbach D, Mao G, Qu F, Bayir H, Fullekrug J, Scheel CH, Wurst W, Schick JA, Kagan VE, Angeli JP, Conrad M. ACSL4 dictates ferroptosis sensitivity by shaping cellular lipid composition. Nat Chem Biol. 2017; 13:91–98. [PubMed: 27842070]
22. Krainz T, Gaschler MM, Lim C, Sacher JR, Stockwell BR, Wipf P. A Mitochondrial-Targeted Nitroxide Is a Potent Inhibitor of Ferroptosis. ACS Cent Sci. 2016; 2:653–659. [PubMed: 27725964]
23. Tait SW, Oberst A, Quarato G, Milasta S, Haller M, Wang R, Karvela M, Ichim G, Yatim N, Albert ML, Kidd G, Wakefield R, Frase S, Krautwald S, Linkermann A, Green DR. Widespread mitochondrial depletion via mitophagy does not compromise necroptosis. Cell Rep. 2013; 5:878–885. [PubMed: 24268776]
24. Narendra D, Tanaka A, Suen DF, Youle RJ. Parkin is recruited selectively to impaired mitochondria and promotes their autophagy. J Cell Biol. 2008; 183:795–803. [PubMed: 19029340]
25. Alberts, B. Molecular biology of the cell. 4. Garland Science; New York: 2002.

26. Yang WS, SriRamaratnam R, Welsch ME, Shimada K, Skouta R, Viswanathan VS, Cheah JH, Clemons PA, Shamji AF, Clish CB, Brown LM, Girotti AW, Cornish VW, Schreiber SL, Stockwell BR. Regulation of ferroptotic cancer cell death by GPX4. Cell. 2014; 156:317–331. [PubMed: 24439385]

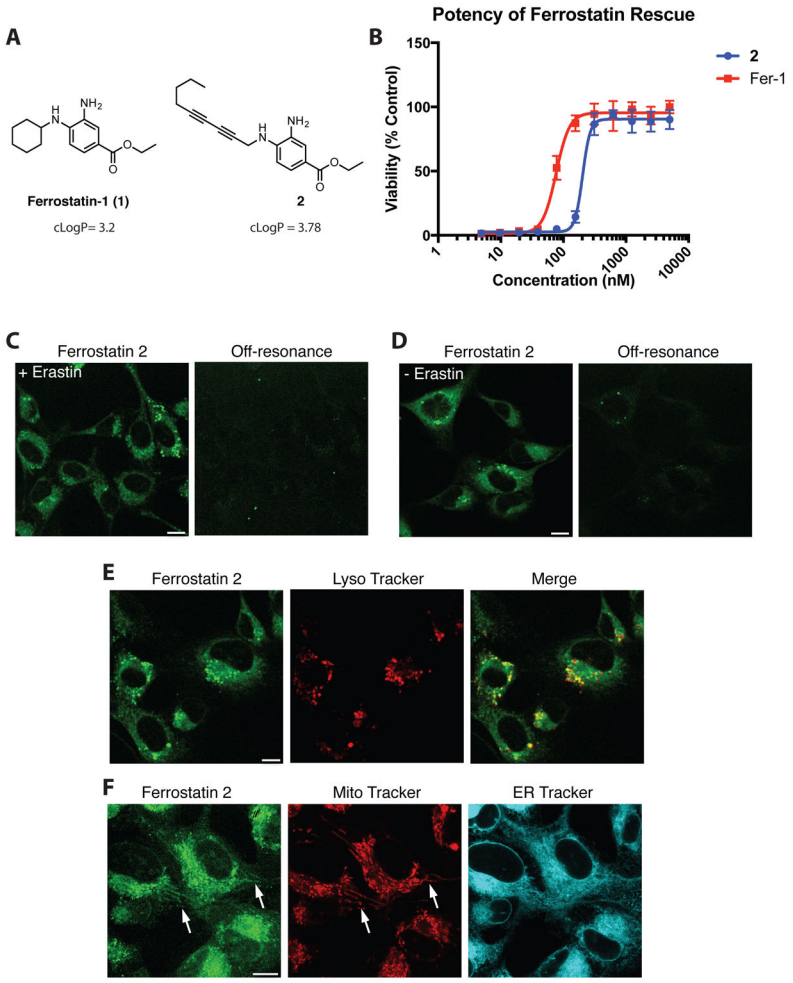

Figure 1.

SRS imaging of ferrostatins in live HT-1080 cells. (A) Structure of ferrostatin-1 (**1**) and diyne ferrostatin (**2**). (B) Potency of ferrostatin analogs in HT-1080 cells treated with erastin (10 μM). Viability was measured 24 h after treatment. (C) SRS images of ferrostatin **2** (10 μM) in live HT-1080 cells treated with erastin (10 μM). Images gathered 6 h after compound addition. (D) SRS image of ferrostatin **2** (10 μM) in live HT-1080 cells in the absence of erastin. Images gathered 6 h after compound addition. (E) Co-localization of signal from live HT-1080 cells treated with erastin and ferrostatin **2** (10 μM each) for 6 h and Lyso Tracker Red (100 nM) for 30 min. (F) SRS or fluorescence signal from live HT-1080 cells treated with erastin and ferrostatin **2** (10 μM each) for 6 h and MitoTracker Deep Red (200 nM) for 30 min, or ERTracker Green (2 μM) for 1 h. Scale bars, 10 μM.

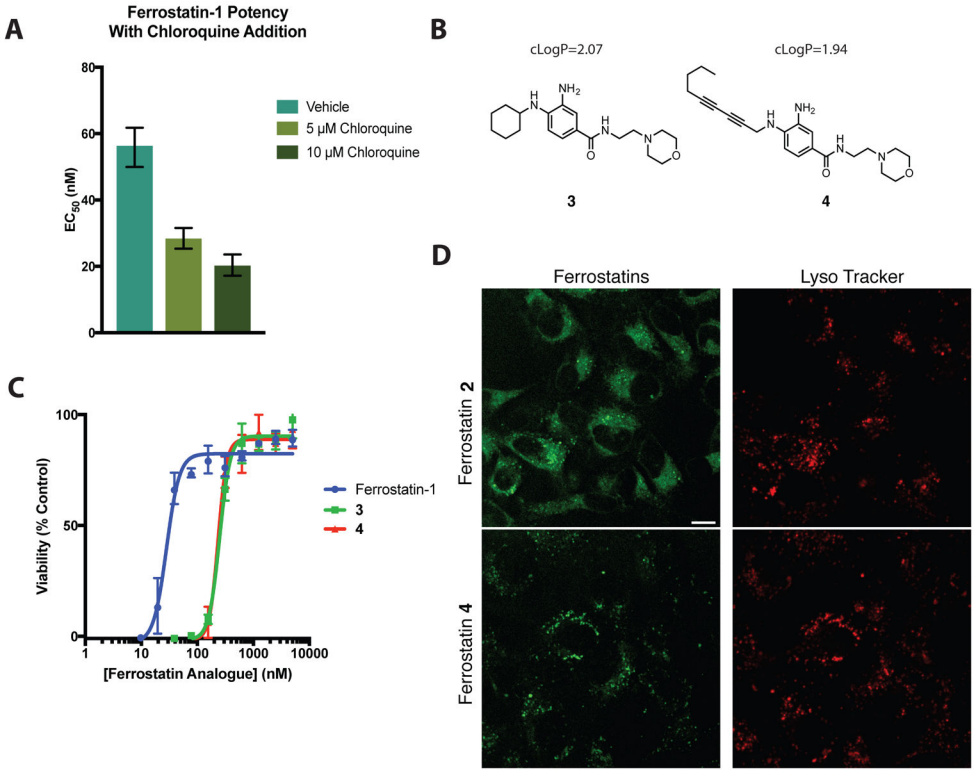

Figure 2.

Accumulation within lysosomes reduces ferrostatin potency. (A) Decreasing EC_{50} of ferrostatin-1 mediated erastin (10 μM) rescue in the presence of 0, 5, and 10 μM chloroquine. Viability was measured at 24 h after compound treatment. Column height represents EC_{50} value with error bars corresponding to the 95% confidence interval. (B) Structure of lysosome-targeted ferrostatin **3** and SRS-compatible lysosome targeted ferrostatin **4**. (C) Potency of ferrostatins in suppressing ferroptosis initiated by erastin (10 μM). (D) Signal in live HT-1080 cells treated with erastin and ferrostatins **2** or **4** (10 μM each, 6 h) and LysoTracker Red (100 nM, 30 min). Scale bars, 10 μM.

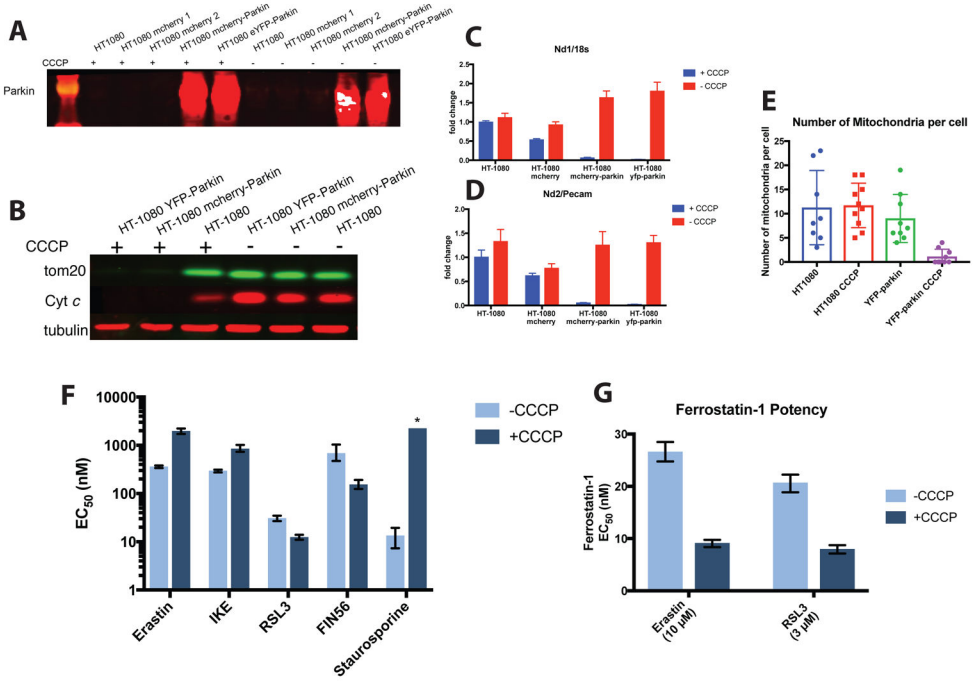

Figure 3.

Cells depleted of mitochondria are still sensitive to ferroptosis inducers and ferrostatins. (A) Western blot of parkin protein levels in wild type and transfected HT-1080 cells in the presence and absence of CCCP. (B) Western blot of tom20 and cytochrome C proteins in wild type, YFP-parkin, and mCherry-parkin transfected HT-1080 cells following treatment with CCCP (12.5 μM) for 48 h. (C and D) Nd1 mRNA abundance (C) and Nd2 mRNA abundance (D) in wild type and transfected cells in the presence or absence of CCCP (12.5 μM for 48 h). (E) Quantification of mitochondria abundance from electron microscopy images in wild type and YFP-parkin transfected HT-1080 cells in the absence and presence of CCCP (12.5 μM for 48 h). (F) Potency of ferroptosis inducers and the apoptosis inducer staurosporine in YFP-parkin expressing HT-1080 cells with (−CCCP) and without (+CCCP) mitochondria. Column height represents EC_{50} value with error bars corresponding to the 95% confidence interval. (G) Potency of ferrostatin-1 in preventing erastin or RSL3 initiated ferroptosis in YFP-parkin expressing HT-1080 cells with (−CCCP) and without (+CCCP) mitochondria. Column height represents EC_{50} value with error bars corresponding to the 95% confidence interval.